



# Use of heated corrugations for propulsion

J.M. Floryan<sup>1,†</sup>, S.A. Aman<sup>1</sup> and S. Panday<sup>1</sup>

<sup>1</sup>Department of Mechanical and Materials Engineering, The University of Western Ontario, London, ON N6A 5B9, Canada

(Received 12 June 2023; revised 3 December 2023; accepted 13 January 2024)

We show that a heating pattern applied to a surface with a corrugation pattern generates a propulsive effect. The same heating pattern applied to a smooth surface creates propulsion through nonlinear thermal streaming associated with pitchfork bifurcation. The combination of groove and heating patterns generates thermal drift, representing a forced response whose magnitude changes with the relative position of both patterns. Thermal drift is always present, while thermal streaming requires sufficiently intense heating. When both effects are active, a change in the relative position of these patterns produces rapid changes in the magnitude of propulsion, resulting in the formation of limit points. The strength of propulsion increases with a decrease in the Prandtl number and with an addition of uniform heating.

**Key words:** general fluid mechanics

## 1. Introduction

The effectiveness of fluid transportation depends on the availability of propulsive devices. These devices take mechanical power from a source and convert it into a propulsive effect. As a wide range of phenomena is utilized for energy conversion, the resulting devices can be classified for the convenience of this discussion as either concentrated or distributed systems. Examples of concentrated propulsion include fans, pumps, jets, propellers, etc. whose analysis and designs attract plenty of attention. Concentrated systems are found in biology, e.g. fish propulsion using flapping foils and bird propulsion using a different form of flapping foils, and have become a subject of intense research in recent years (Wu 2011; Floryan, Burren & Smits 2018; Mannam & Krishnankutty 2019; Smits 2019). Distributed propulsion relies on the interaction between a solid surface and the adjacent fluid and is frequently used by small-scale biological organisms, e.g. snail locomotion

† Email address for correspondence: [floryan@uwo.ca](mailto:floryan@uwo.ca)

(Chan *et al.* 2005; Lee *et al.* 2008), cilia and flagella (Taylor 1951; Blake & Sleight 1974; Katz 1974; Brennen & Winet 1977; Lauga 2016), etc. Its use can also be found in large systems, e.g. bowel movements, although this is less common. Analysis and development of distributed systems for technical applications have been focused on the peristaltic effect, starting with the work of Shapiro and Fung and their co-workers (Fung & Yih 1968; Shapiro *et al.* 1969; Jaffrin & Shapiro 1971). Ali *et al.* (2020) provide a recent review. These analyses considered long slow waves, such as those encountered in biological systems. Current results demonstrate that fast, short peristaltic waves are more effective in providing a route to novel applications (Floryan *et al.* 2021; Floryan & Haq 2022; Haq & Floryan 2022).

Concentrated and distributed propulsions can be used simultaneously to achieve a performance not accessible to any of them individually. Active flow control can be viewed as a form of distributed propulsion, where improved performance is achieved by spending energy on reducing friction (Hoepffner & Fukagata 2009). There is a vast amount of literature on active control, but without referring to it as the development of distributed propulsion systems (Cattafesta & Sheplak 2011). The objectives of active control were narrowly defined as a search for net energy savings, i.e. energy savings larger than the energy cost required to achieve them, rather than a search for propulsion augmentation techniques. Such savings are not achievable in smooth conduits modified by wall transpiration (Bewley 2009); indications are that the situation can differ in non-smooth conduits (Floryan 2023). Results in the literature demonstrate that proper surface topography modifications reduce resistance (Walsh 1983; Fukagata *et al.* 2009; Mohammadi & Floryan 2013*a,b*, 2015; Moradi & Floryan 2013). It is also possible to produce chaotic stirring at an energy cost less than required to maintain the same flow rate in a smooth conduit (Gepner & Floryan 2020).

Forcing (actuation) patterns imposed on the contact surface between fluid and solid create distributed propulsion. These actuations reduce the wall shear acting on the fluid and increase its velocity relative to the solid boundary. Numerous concepts have been investigated, e.g. plasma-based actuators (Inasawa *et al.* 2013) and piezo-driven actuators (Fukunishi & Ebina 2001). See also the review provided by Cattafesta & Sheplak (2011). More recent contributions were focused on the thermal drift created by the interaction of groove and heating patterns (Abtahi & Floryan 2017; Inasawa *et al.* 2021) through the pattern interaction effect (Floryan & Inasawa 2021) on pumping driven by thermal drift (Floryan, Haq & Panday 2022), on propulsion driven by nonlinear thermal streaming (Floryan, Panday & Aman 2022) and on nonlinear streaming created by distributed wall transpiration (Jiao & Floryan 2021*a,b*).

Body forces distributed within the fluid volume can create distributed propulsion. Heating patterns produce a propulsive force and reduce viscous friction simultaneously (Hossain *et al.* 2012; Floryan & Floryan 2015; Hossain & Floryan 2016). Utilizing available waste heat reduces the energy cost required by such heating. While groove patterns generally increase friction (unless one uses unique shapes), a judicious combination of heating and groove patterns can reduce pressure losses (Hossain & Floryan 2016; Floryan, Shadman & Hossain 2018). Sound represents another form of volume actuation, but little is known about its effectiveness (Kato *et al.* 1997).

This paper describes the use of heated grooves to generate distributed propulsion. The model problem used in the analysis is described in § 2. Section 3 discusses the thermal drift effect and provides its essential characterization. Section 4 reviews the properties of nonlinear thermal streaming. Propulsion, when both effects are simultaneously active, is discussed in § 5. Section 6 provides a summary of the main conclusions.

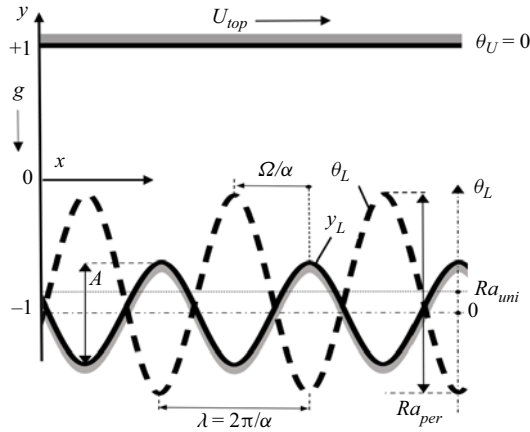


Figure 1. Schematic diagram of the flow system.

## 2. Problem formulation

Consider two horizontal plates with a gap between them filled with a fluid, as shown in figure 1. The upper plate is smooth, while the lower one has sinusoidal corrugations, resulting in the gap geometry of the form

$$y_L^*(x^*) = -h^* + 0.5 A^* \cos(\alpha^* x^*), \quad y_U^*(x^*) = h^*, \quad (2.1a,b)$$

where the subscripts  $L$  and  $U$  refer to the lower and upper plates, respectively,  $A^*$  is the (peak to bottom) amplitude of the groove,  $\alpha^*$  is its wavenumber and stars identify dimensional quantities. The gap extends to  $\pm\infty$  in the  $x^*$ -direction, its mean opening is  $2h^*$  and it is periodic with wavelength  $\lambda^* = 2\pi/\alpha^*$ . The gravitational acceleration  $g^*$  is acting in the negative  $y^*$ -direction. The fluid is assumed to have a thermal conductivity  $k^*$ , specific heat  $c^*$ , thermal diffusivity  $\kappa^* = k^*/\rho^*c^*$ , kinematic viscosity  $\nu^*$ , dynamic viscosity  $\mu^*$ , thermal expansion coefficient  $\Gamma^*$  and variations of its density  $\rho^*$  follow the Boussinesq approximation. Conditions required for the use of this approximation are discussed by Tritton (1977). Results of experiments for thermal conditions similar to those used in this analysis (Inasawa *et al.* 2019, 2021; Floryan & Inasawa 2021) demonstrate that the Boussinesq approximation captures well the fluid response. These experiments included qualitative (flow topology) and quantitative (velocity measurements) comparisons with the theoretical model.

The upper plate is free to move within its plane, and the lower plate is stationary. The upper plate does not move in the case of an isothermal system, as no mechanism is available to generate a propulsive force. The introduction of patterned heating produces convection in the slot, and it is interesting to determine if this convection can force movement of the upper plate. We assume that the heating applied to the lower plate results in a simple sinusoidal temperature distribution while the upper plate is kept isothermal, i.e.

$$T_L^*(x^*) = T_{mean,L}^* + 0.5 T_{per}^* \cos(\alpha^* x^* + \Omega^*), \quad T_U^*(x^*) = T_U^*, \quad (2.2a,b)$$

where the subscripts ‘mean’ and ‘per’ refer to the mean and periodic parts, respectively,  $T_{per}^*$  is the peak-to-peak amplitude of the periodic component and  $\Omega^*$  denotes the phase shifts between the heating and groove patterns. We use  $T_U^*$  for reference with all material

properties and define the relative temperature  $\theta^* = T^* - T_U^*$  to get

$$\theta_L^*(x) = \theta_{uni}^* + 0.5 \theta_{per}^* \cos(\alpha^* x^* + \Omega^*), \quad \theta_U^*(x) = 0, \quad (2.3a,b)$$

where  $\theta_{uni}^* = T_{uni}^* = T_{mean,L}^* - T_U^*$ ,  $\theta_{per}^* = T_{per}^*$ . Finally, we use half of the mean gap height  $h^*$  as the length scale and  $\kappa^* \nu^* / (g^* \Gamma^* h^{*3})$  as the temperature scale to find the dimensionless expressions for the geometry and temperatures of the form

$$y_L(x) = -1 + 0.5A \cos(x), \quad y_U(x) = 1, \quad (2.4a,b)$$

$$\theta_L(x) = Ra_{uni} + 0.5Ra_{per} \cos(\alpha x + \Omega), \quad \theta_U(x) = 0, \quad (2.5a,b)$$

where  $Ra_{uni} = g^* \Gamma^* h^{*3} T_{uni}^* / (\kappa^* \nu^*)$  is the uniform Rayleigh number measuring the intensity of the uniform heating component and  $Ra_{per} = g^* \Gamma^* h^{*3} T_{per}^* / (\kappa^* \nu^*)$  is the periodic Rayleigh number measuring the intensity of the periodic heating component. Determination of whether the heating can create a movement of the upper plate requires a solution of the field equations of the form

$$\frac{\partial u}{\partial x} + \frac{\partial v}{\partial y} = 0, \quad u \frac{\partial u}{\partial x} + v \frac{\partial u}{\partial y} = -\frac{\partial p}{\partial x} + \nabla^2 u, \quad (2.6a,b)$$

$$u \frac{\partial v}{\partial x} + v \frac{\partial v}{\partial y} = -\frac{\partial p}{\partial y} + \nabla^2 v + Pr^{-1} \theta, \quad u \frac{\partial \theta}{\partial x} + v \frac{\partial \theta}{\partial y} = Pr^{-1} \nabla^2 \theta, \quad (2.6c,d)$$

where  $(u, v)$  are the velocity components in the  $(x, y)$  directions, respectively, scaled with  $U_v^* = \nu^* / h^*$  as the velocity scale,  $p$  stands for the pressure scaled with  $\rho^* U_v^{*2}$  as the pressure scale and  $Pr = \nu^* / \kappa^*$  denotes the Prandtl number. These equations are subject to the following boundary conditions:

$$y = -1 + 0.5A \cos(x): u = v = 0, \quad \theta = Ra_{uni} + 0.5Ra_{per} \cos(\alpha x + \Omega), \quad (2.7a-c)$$

$$y = 1: \left. \frac{\partial u}{\partial y} \right|_{mean} = 0, \quad u_{per} = 0, \quad v = 0, \quad \theta = 0. \quad (2.7d-g)$$

One must impose constraints in the form of

$$\left. \frac{\partial p}{\partial x} \right|_{mean} = 0 \quad (2.8)$$

to prevent any external pressure gradient from affecting the fluid movement. If convection generates a mean shear stress at the upper plate, then this plate accelerates until it reaches velocity  $U_{top}$ , which eliminates this stress – all forces acting on the upper plate must balance out, so, since the only permitted force is due to shear, the mean shear must be zero. The periodic components of shear do not matter as they cancel out over one period. The velocity of the upper plate  $U_{top}$  is not known *a priori* – it is determined from the known solution during the postprocessing.

Identification of the plate driving forces requires evaluation of the surface forces acting on the plates. The stress vector at the lower plate  $\sigma_L$  is expressed as

$$\sigma_L = [\sigma_{x,L} \quad \sigma_{y,L}] = [n_{x,L} \quad n_{y,L}] \begin{bmatrix} 2 \frac{\partial u}{\partial x} - p & \frac{\partial u}{\partial y} + \frac{\partial v}{\partial x} \\ \frac{\partial u}{\partial y} + \frac{\partial v}{\partial x} & 2 \frac{\partial v}{\partial y} - p \end{bmatrix}, \quad (2.9)$$

*Use of heated corrugations for propulsion*

where  $\mathbf{n}_L = (n_{x,L}, n_{y,L}) = N_L(dy_L/dx, -1)$ ,  $N_L = [1 + (dy_L/dx)^2]^{-1/2}$ , is the normal unit vector pointing outwards. The  $x$ -component of this vector has the form

$$\sigma_{x,L} = \sigma_{xv,L} + \sigma_{xp,L} = N_L \left[ 2 \frac{dy_L}{dx} \frac{\partial u}{\partial x} - \left( \frac{\partial u}{\partial y} + \frac{\partial v}{\partial x} \right) \right] - N_L \frac{dy_L}{dx} p, \quad (2.10)$$

where  $(\sigma_{xv,L}, \sigma_{xp,L})$  denote the viscous and pressure contributions, respectively. The  $x$ -component of the total force  $F_{x,L}$  acting on the fluid at the lower plate per unit length has the form

$$F_{x,L} = F_{xv,L} + F_{xp,L} = \lambda^{-1} \int_0^\lambda \left[ 2 \frac{dy_L}{dx} \frac{\partial u}{\partial x} - \left( \frac{\partial u}{\partial y} + \frac{\partial v}{\partial x} \right) \right] dx - \lambda^{-1} \int_0^\lambda \frac{dy_L}{dx} p dx = 0, \quad (2.11)$$

where  $F_{xp,L}$  and  $F_{xv,L}$  stand for the pressure and viscous contributions, which must be equal and opposite. Similar expressions for the upper plate have the form

$$\sigma_{x,U} = \sigma_{xv,U} = \frac{du}{dy} \Big|_{y=1}, \quad F_{x,U} = F_{xv,U} = \lambda^{-1} \int_0^\lambda \frac{du}{dy} \Big|_{y=1} dx = 0, \quad (2.12a,b)$$

and the total force must be null.

System (2.6)–(2.8) must be solved numerically with sufficient accuracy to provide a data quality suitable for analysing the effects of geometric irregularities and heating and their interactions. Modelling the irregularities requires using techniques able to accurately handle many geometries with an acceptable cost. The spectrally accurate immersed boundary method accomplishes this, as it provides both the necessary geometric flexibility and accuracy and the ability to handle many geometries with a minimum labour cost.

We express the field equations in terms of the stream function defined in the usual manner, i.e.  $u = \partial\psi/\partial y$ ,  $v = -\partial\psi/\partial x$ , and normalized with condition  $\psi(y_L) = 0$ . Further, we capture the  $x$ -dependences of this function, as well as temperature  $\theta$ , by expressing them as Fourier expansions based on the wavenumber  $\alpha$ . Then we substitute these expansions into the field equations and separate the Fourier modes formulating nonlinear, ordinary differential equations for the modal functions. We express the modal functions using Chebyshev expansions and employ the Galerkin projection method to construct algebraic equations for the expansion coefficients. The irregular shape of the lower plate is accommodated using the spectrally accurate immersed boundary conditions concept (Szumarski & Floryan 1999; Husain & Floryan 2008, 2010; Husain *et al.* 2009). The resulting constraints expressing the flow and boundary conditions along the lower corrugated plate and boundary conditions along the smooth upper plate are accommodated using the tau method. The nonlinear algebraic equations resulting from the discretization process are solved using a fixed-point iterative technique. The discretization process provided spectral accuracy with the absolute error controlled by the number of Chebyshev polynomials and Fourier modes used in the computations. We determined that using 15 Fourier modes and 50 Chebyshev polynomials provided a minimum of five digit accuracy for all quantities of interest. The reader can find algorithm details in Panday & Floryan (2021).

The heating activates different physical mechanisms. We begin the discussion by presenting these mechanisms in detail and then discuss the propulsion generated by these effects.

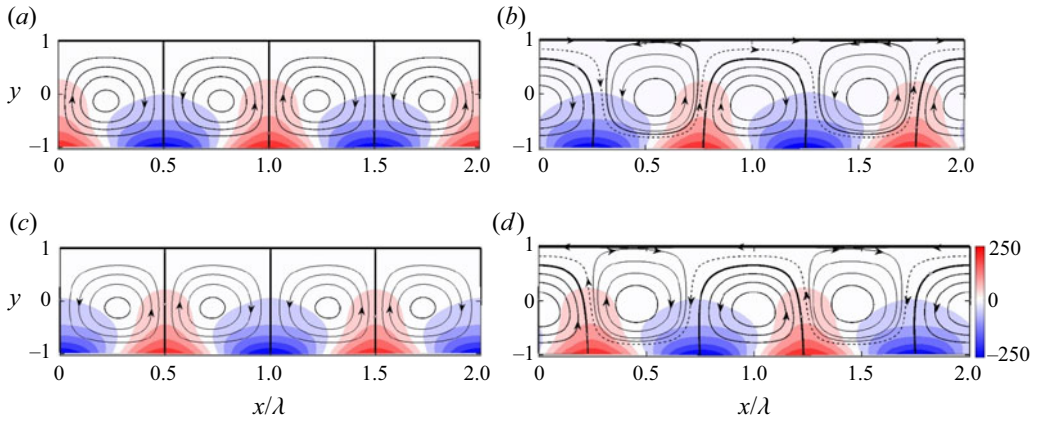


Figure 2. Flow and temperature fields for  $\alpha = 2$ ,  $A = 0.025$ ,  $Ra_{umi} = 0$ ,  $Ra_{per} = 500$  (a–d) corresponding to  $\Omega = 0, \pi/2, \pi, 3\pi/2$ , respectively. Dashed lines identify stream tubes carrying fluid in the horizontal direction.

### 3. Thermal drift effect

We begin the discussion with a description of the thermal drift effect. If the upper plate does not experience any external resistance, viscous shear associated with convective motion may accelerate this plate until it reaches a velocity  $U_{top}$  – the mean shear becomes zero under this condition.

Typical velocity and temperature fields are illustrated in figure 2. When the hot spots are located at the groove crests ( $\Omega = 0$ ), the flow topology is made of counter-rotating pairs of rolls with the fluid moving upwards above the hot spots (figure 2a). When the hot spots are located at the groove bottoms ( $\Omega = \pi$ ), the flow field has a similar structure (figure 2c). All other positions of the hot spots result in the formation of a net horizontal flow directed either to the right ( $0 < \Omega < \pi$ ) or to the left ( $\pi < \Omega < 2\pi$ ), as illustrated in figure 2(b,d), respectively. The flow direction is dictated by the relative position of the heating and groove patterns and represents a special form of thermal drift (Abtahi & Floryan 2017, 2018; Inasawa *et al.* 2021) driven by the pattern interaction effect (Floryan & Inasawa 2021).

The strength of the drift pulling the upper plate is quantified in terms of the velocity  $U_{top}$ . Typical variations of  $U_{top}$  as a function of the phase shift  $\Omega$  illustrated in figure 3(a) demonstrate that positioning the hot spots either at  $\Omega = \pi/2$  or at  $\Omega = 3\pi/2$  produces the fastest plate movement. This speed increases proportionally to the groove amplitude, as illustrated in figure 3(b).

Figure 4(a) illustrates the distribution of the  $x$ -component of the pressure force  $\sigma_{xp,L}$  acting on the fluid at the lower plate that drives the fluid in the horizontal direction. The form of the pressure field is dictated by the convection pattern, whose structure, in turn, is dictated by the heating pattern. As this pattern moves relative to the grooves, the projection of the pressure field onto the surface topography changes, producing  $\sigma_{xp,L}$  of different magnitudes and directions – this projection is responsible for horizontal fluid movement (Abtahi & Floryan 2017). The convective motion generates an  $x$ -component of the shear stress  $\sigma_{xv,L}$  at the grooved plate with large periodic  $x$ -variations (see figure 4b). The mean value of the shear stress  $F_{xv,L}/\lambda$  must be equal to the mean value of the pressure force  $F_{xp,L}/\lambda$  as the upper plate does not support any forces.

Uniform heating applied to the lower plate increases the plate velocity as the intensity of convection increases, while uniform cooling produces the opposite effect, as illustrated



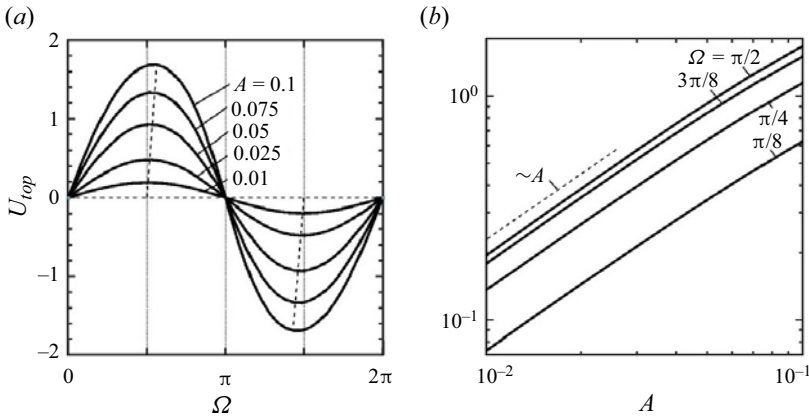


Figure 3. Variation of the upper plate velocity  $U_{top}$  (a) as a function of the phase shift  $\Omega$  and (b) as a function of the groove amplitude  $A$  for  $\alpha = 2$ ,  $Pr = 0.71$ ,  $Ra_{per} = 500$ ,  $Ra_{umi} = 0$ . Thin dotted lines in (a) show  $\Omega$  giving rise to maximum  $U_{top}$  and in (b) identify the character of the asymptotic variations for  $A \rightarrow 0$ .

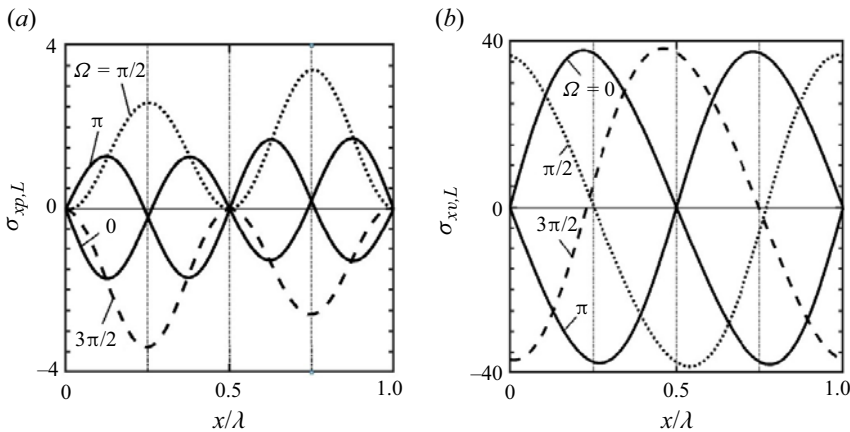


Figure 4. Distributions of (a) the  $x$ -component of the pressure force  $\sigma_{xp,L}$  and (b) the  $x$ -component of the shear force  $\sigma_{xv,L}$  acting on the fluid at the lower plate for  $\alpha = 2$ ,  $A = 0.025$ ,  $Ra_{per} = 500$ ,  $Ra_{umi} = 0$ ,  $Pr = 0.71$  and  $\Omega = 0, \pi/2, \pi, 3\pi/2$ . The total forces are  $F_{xp,L} = 0, 1.49, 0, -1.49$ ,  $F_{xv,L} = 0, -1.49, 0, 1.49$  for  $\Omega = 0, \pi/2, \pi, 3\pi/2$ , respectively.

in [figure 5\(a\)](#). Reduction of the Prandtl number increases the strength of convection as mixing associated with convective motion is less effective in reducing horizontal temperature gradients (Hossain & Floryan 2013, 2022), leading to an increase of  $U_{top}$ , while its reduction has the opposite effect, as illustrated in [figure 5\(b\)](#).

The stability of thermal drifts was assessed using the technique outlined in [Appendix A](#). No unstable eigenvalues have been found, which suggests that thermal drifts are stable in the range of parameters of interest in this analysis.

#### 4. Nonlinear thermal streaming effect

If the upper plate does not experience external resistance and the lower plate is smooth, sufficiently intense periodic heating may generate plate movement through nonlinear thermal streaming (Floryan 2023). The fluid motion has the form of counter-rotating

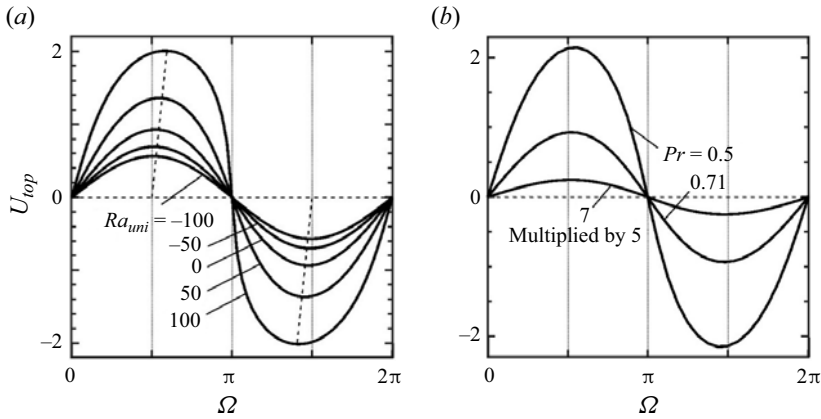


Figure 5. Variations of the upper plate velocity  $U_{top}$  as a function of the phase shift  $\Omega$  for (a)  $Pr = 0.71$ ,  $Ra_{uni} = -100, -50, 0, 50, 100$ , and for (b)  $Ra_{uni} = 0, Pr = 0.5, 0.71, 7$ . In both cases,  $\alpha = 2, A = 0.05$  and  $Ra_p = 500$ . Thick dashed lines in (a) show variations of the maximum of  $|U_{top}|$  as a function of  $\Omega$ . Term ‘multiplied by 5’ means that the quantity of interest was multiplied by a factor of 5 before plotting.

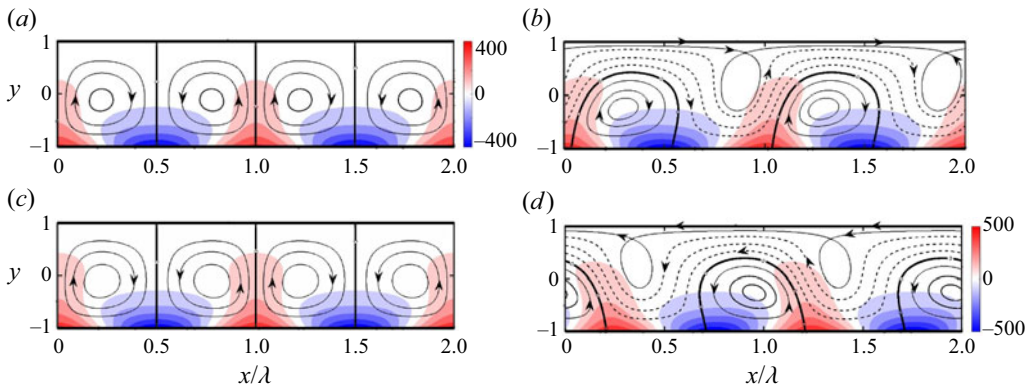


Figure 6. Flow and temperature fields for  $\alpha = 2.1, A = 0, Ra_{uni} = 0$  and  $Ra_{per} = (a) 884, (b) 1000, (c) 1000, (d) 1000$ . Dashed lines identify stream tubes carrying fluid in the horizontal direction.

rolls, as illustrated in figure 6. These rolls generate viscous stresses at the upper plate. If plumes of heated fluid flow straight upwards, the flow exhibits left/right symmetry, and the resulting stress has no mean component. A sufficiently strong plume may tilt either to the left or right, producing a non-zero mean stress, which results in movement of the upper plate – the plate accelerates until the mean shear is eliminated.

The plate movement results from a system bifurcation, as illustrated in figure 7. The heating intensity, as measured by  $Ra_{per,cr}$ , must reach a minimum level that strongly depends on the heating wavenumber – the minimum corresponds to  $Ra_{per,cr} \approx 900$ , it occurs at  $\alpha \approx 2.1$ , rapidly increasing when the heating wavelength is too short or too long (see figure 7). The value of  $Ra_{per,cr}$  rapidly increases when the Prandtl number increases as convection reduces the horizontal temperature gradients required to initiate this effect (see figure 7b). An addition of uniform heating minimizes the intensity of periodic heating required to produce bifurcation. In contrast, constant cooling has the opposite effect (see figure 7c).



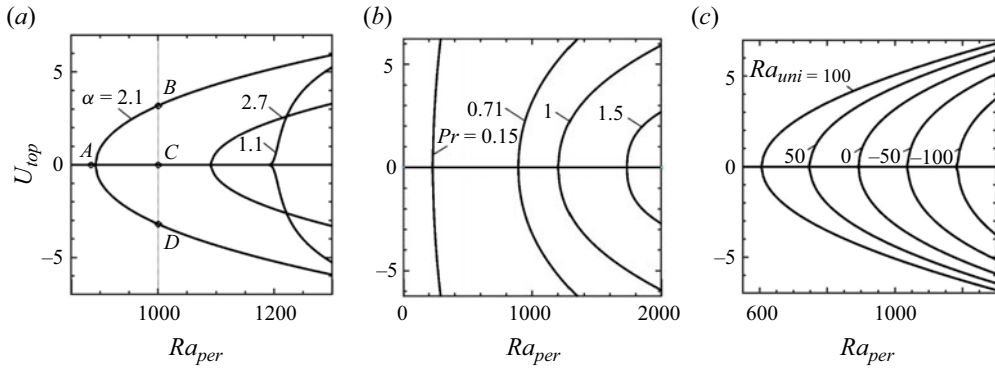


Figure 7. Variations of the upper plate velocity  $U_{top}$  (a) as a function of  $Ra_{per}$  for  $Ra_{uni} = 0$ ,  $Pr = 0.71$ ,  $\alpha = 1.1, 2.1, 2.7$ , (b) as a function of  $Ra_{per}$  for  $Ra_{uni} = 0$ ,  $\alpha = 2.1$ ,  $Pr = 0.15, 0.71, 1, 1.5$  and (c) as a function of  $Ra_{per}$  for  $\alpha = 2.1$ ,  $Pr = 0.71$ ,  $Ra_{uni} = 100, 50, 0, -50, -100$ . Groove amplitude  $A = 0$  in all cases. The critical conditions for  $\alpha = 1.1, 2.1, 2.7$  in (a) are  $Ra_{per,cr} = 1206, 891.25, 1091.25$ , respectively. The critical conditions for  $Pr = 0.15, 0.71, 1, 1.5$  in (b) are  $Ra_{per,cr} = 228.5, 891.25, 1203.33, 1730$ , respectively. The critical conditions for  $Ra_{uni} = 100, 50, 0, -50, -100$  in (c) are  $Ra_{per,cr} = 605.83, 747.5, 891.25, 1038.33, 1185$ , respectively. All critical conditions were determined using stability analysis.

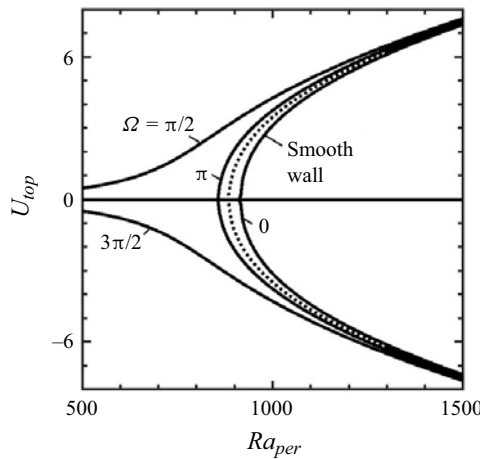


Figure 8. Variations of the upper plate velocity  $U_{top}$  as a function of the heating intensity  $Ra_{per}$  for  $\Omega = 0, \pi/2, \pi, 3\pi/2$ ,  $A = 0.025$ ,  $Pr = 0.71$ ,  $Ra_{uni} = 0$ ,  $\alpha = 2$ . Dotted lines provide the plate velocity achieved with smooth plates. The critical conditions are  $Ra_{per,cr} = 914, 857.5$  for  $\Omega = 0, \pi$  for a grooved plate, respectively, and  $Ra_{per,cr} = 884.5$  for the smooth plate. These conditions were determined using stability theory.

### 5. Combined effect

When the thermal drift and streaming effects are active, the combined effect occurs for a sufficiently high heating intensity. One can estimate the minimum heating required to activate the streaming for the grooved plate by placing hot spots either at the groove peaks or at the groove troughs, as this eliminates thermal drift. Results in figure 8 demonstrate relatively minor changes in critical conditions to those found in the case of a smooth plate. The same results also illustrate different responses when the hot spots are placed at the groove troughs and the groove peaks.

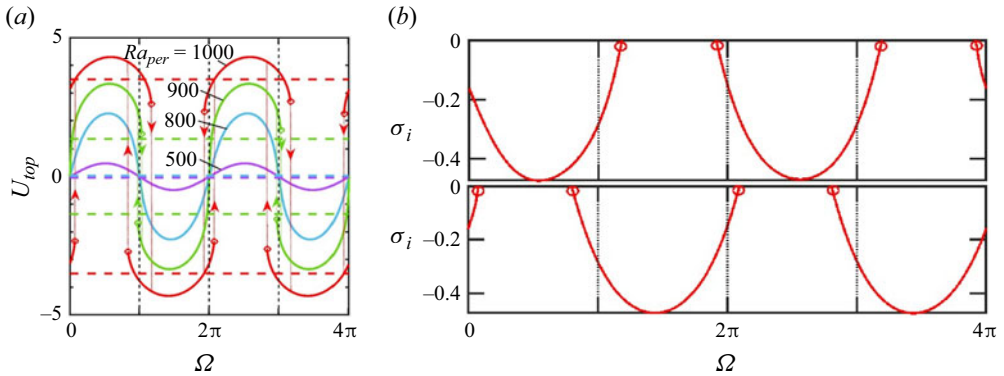


Figure 9. (a) Variations of the upper plate velocity  $U_{top}$  as a function of the phase shift  $\Omega$  for  $\alpha = 2$ ,  $A = 0.025$ ,  $Pr = 0.71$ ,  $Ra_{uni} = 0$  and  $Ra_{per} = 500, 800, 900, 1000$ . Circles identify limit points. The dotted lines provide the plate velocity achieved with smooth plates. (b) Variations of the disturbance amplification rate  $\sigma_i$  (see Appendix A for definition) as a function of the phase shift  $\Omega$  for flow conditions corresponding to red lines in (a). These disturbances are characterized by frequency  $\sigma_r = 0$  (see Appendix A for definition).

The combined system response depends on the relative position of the heating and groove patterns, as illustrated in figure 9(a). The value of  $U_{top}$  varies as a function of phase difference  $\Omega$  in a regular, nearly sinusoidal manner for  $Ra_{per} = 500$ , which means that the flow response is driven by thermal drift and nonlinear streaming plays no role. Increase heating intensity to  $Ra_{per} = 800$ , i.e. an increase of a factor of 1.6, results in a rise in the maximum possible  $U_{top}$  by a factor of 4.7 while retaining its sinusoidal variations with  $\Omega$ . When heating intensity is further increased to  $Ra_{per} = 900$ , variations of  $U_{top}$  remain regular, except when the phase difference is near  $\Omega = \pi$ , which corresponds to hot spots near the groove troughs. Nonlinear streaming becomes activated, leading to the appearance of limit points in variations of  $U_{top}$  as a function of  $\Omega$  – for such conditions, a slight change of  $\Omega$  can change the direction of plate movement. System response shows hysteresis – when  $\Omega$  increases towards  $\Omega = \pi$  and crosses the value of 3.23,  $U_{top}$  jumps from  $U_{top} = 1.53$  to  $U_{top} = -2.46$ . When  $\Omega$  decreases back,  $U_{top}$  does not jump back until the phase shift reaches a value of  $\Omega = 3.06$ , when it jumps from  $U_{top} = -1.67$  to  $U_{top} = 2.43$ . The hysteresis loop is relatively narrow, i.e. it occurs between  $\Omega = 3.06$  and  $\Omega = 3.23$ , with  $U_{top}$  being positive at the upper side of the loop and negative at the lower side. Increasing the heating intensity to  $Ra_{per} = 1000$  results in the formation of additional limit points near  $\Omega = 0$ , which correspond to hot spots near the groove peaks with another hysteresis loop forming there and a widening of the hysteresis loop near  $\Omega = \pi$ . Stability analysis (see Appendix A for details) demonstrates that the formation of limit points corresponds to the loss of stability of a particular branch of the bifurcation diagram (figure 9b). No stationary unstable states were found past the limit points, which suggests that only non-stationary states may exist under such conditions.

Evolution of  $U_{top}$  as a function of  $Ra_{per}$  near  $\Omega = 0$ , which corresponds to hot spots near the groove peaks, is illustrated in figure 10(a). Using  $\Omega = 0$  results in a symmetric pitchfork bifurcation, i.e. the upper plate moves either to the right or to the left in the same manner. Placement of the hot spot very close to the groove peak and on its left side ( $\Omega = 0.08$ ) produces plate movement to the right, with  $U_{top}$  increasing monotonically with  $Ra_{per}$ , i.e. no bifurcation takes place. A separate solution branch corresponding to the plate moving to the left appears when  $Ra_{per} > 850$ . This branch does not connect to the branch describing plate movement to the right – it ends at a limit point at  $Ra_{per} = 956$

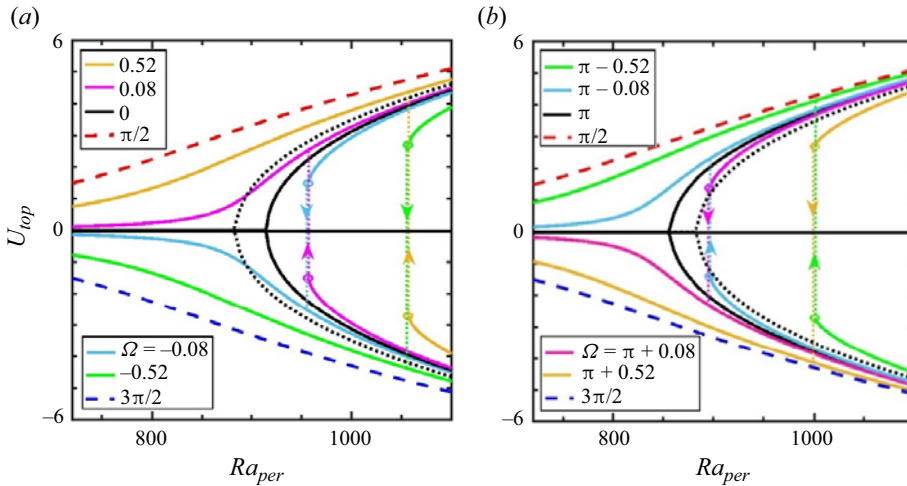


Figure 10. Variations of the upper plate velocity  $U_{top}$  as a function of the heating intensity  $Ra_{per}$  for (a)  $\Omega$  near 0, i.e.  $\Omega = -0.52, -0.08, 0, 0.08, 0.52$ , and (b)  $\Omega$  near  $\pi$ , i.e.  $\Omega = \pi - 0.52, \pi - 0.08, \pi + 0.08, \pi + 0.52$ . All results are for  $A = 0.025, \alpha = 2, Pr = 0.71, Ra_{uni} = 0$ . Circles identify limit points. The dotted lines provide the plate velocity achieved with smooth plates. The critical conditions determined using stability theory are  $Ra_{per,cr} = 910, 855$  for  $\Omega = 0, \pi$  for a grooved plate, respectively, and  $Ra_{per,cr} = 880$  for the smooth plate. Dashed lines provide data for  $\Omega = \pi$  (red) and  $\Omega = 3\pi/2$  (blue).

with  $U_{top} = -1.49$ . Moving the hot spot further away to the left ( $\Omega = 0.52$ ) produces a similar response but with  $U_{top}$  varying with  $Ra_{per}$  in a more regular manner and with a new solution branch forming at a larger  $Ra_{per}$ , i.e. the limit point of the new branch is at  $Ra_{per} = 1056$  with  $U_{top} = -2.71$ . Placing a hot spot on the right side of the groove peak ( $\Omega = -0.08$ ) forces plate movement to the right with a new solution branch corresponding to negative  $U_{top}$  appearing at a limit point  $Ra_{per} = 956$  and  $U_{top} = 1.49$ . Moving the hot spot further away ( $\Omega = -0.52$ ) moves the limit point to  $Ra_{per} = 956$  and  $U_{top} = -1.49$ .

Variations of  $U_{top}$  as a function of  $Ra_{per}$  near  $\Omega = \pi$ , which correspond to hot spots located near the groove troughs, are qualitatively similar to those observed for  $\Omega$  near 0 (see figure 10b). Using  $\Omega = \pi$  leads to a symmetric pitchfork bifurcation. Moving the hot spot to the left of the trough ( $\Omega = 0.08$ ) produces negative  $U_{top}$ , which is a monotonic function of  $Ra_{per}$ . A second branch, corresponding to positive  $U_{top}$ , appears at  $Ra_{per} = 896$  with  $U_{top} = 1.39$ . Moving the hot spots further away to the left ( $\Omega = 0.52$ ) produces more regular variations of  $U_{top}$  as a function of  $Ra_{per}$ , with the second branch originating at  $Ra_{per} = 1000$  with  $U_{top} = 2.7$ . Moving the hot spots to the right produces a near mirror image of flow response with limit points being at  $Ra_{per} = 896$  and  $U_{top} = -1.39$  for  $\Omega = -0.08$  and  $Ra_{per} = 1000$  and  $U_{top} = -2.7$  for  $\Omega = -0.52$ .

Comparisons of the data displayed in figures 8–10 show regular variations of  $U_{top}$  as a function of  $Ra_{per}$  for  $Ra_{per} < \sim 800$ , where thermal drift dominates, and regular variations for  $Ra_{per} > \sim 1100$  where, depending on  $\Omega$ , either nonlinear streaming or thermal drift dominates, producing a nearly identical system response. The system response exhibits somewhat unpredictable but significant changes of  $U_{top}$ , including changes of direction for  $Ra_{per}$  varying between these limits.

The effectiveness of thermal drift increases proportionally to the groove amplitude, as illustrated in figure 3(b). When thermal streaming is active, variations of  $U_{top}$  with  $A$  become complex and change with  $\Omega$  and  $Ra_{per}$  as illustrated in figure 11. Figure 11(a) shows the system response for  $Ra_{per} = 900$ , which is just above the critical heating of

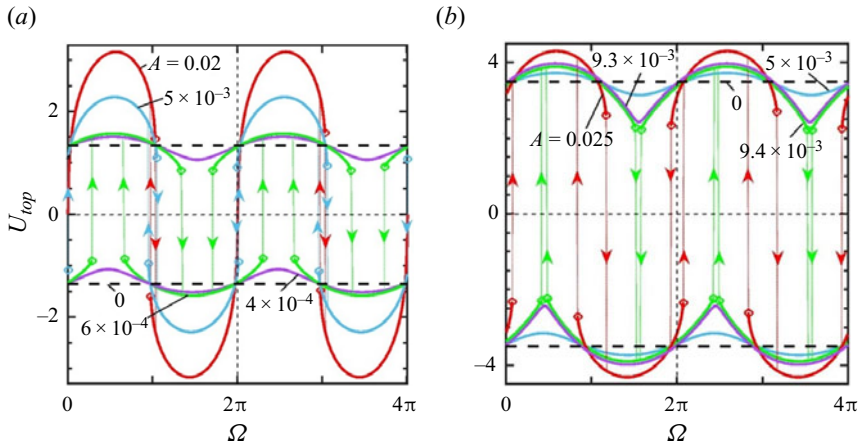


Figure 11. Variations of the upper plate velocity  $U_{top}$  as a function of the phase shift  $\Omega$  for (a)  $Ra_{per} = 900$ ,  $A = 0, 0.001, 0.005, 0.02$ , and (b) for  $Ra_{per} = 1000$ ,  $A = 0, 0.005, 0.0093, 0.0094, 0.025$ . All results are for  $\tau = 2$ ,  $Ra_{umi} = 0$  and  $Pr = 0.71$ . Circles identify limit points. Black dashed lines provide the plate velocity achieved with smooth plates. Positions of limit points were determined using stability theory.

$Ra_{per} = 880$  for a smooth plate. No bifurcation occurs at  $A = 0.0004$ , but one occurs at  $A = 0.0006$ , producing wide hysteresis loops. Further increase of the amplitude to  $A = 0.005$  dramatically narrows down the hysteresis loop. Further increase to  $A = 0.02$  appears to change the magnitude of  $U_{top}$  but does not affect the size of the hysteresis loop. Figure 11(b) illustrates what happens when heating corresponds to  $Ra_{per} = 1000$ . No bifurcation occurs for  $A = 0.005$  and  $A = 0.0093$ , but one is formed when the amplitude reaches  $A = 0.0094$ . The results show that the amplitude must increase by a factor of nearly 10 to produce bifurcation when heating increases from  $Ra_{per} = 900$  to  $Ra_{per} = 1000$ . The hysteresis loop is very narrow at  $A = 0.0094$  but significantly widens when the amplitude increases to  $A = 0.025$ , which demonstrates a trend opposite to that observed for  $Ra_{per} = 900$ .

Uniform heating strengthens thermal drift (see figure 5a) and reduces the critical Rayleigh number required for the onset of thermal streaming (see figure 7c). Effects of adding uniform heating when both effects are active are illustrated in figure 12. In general, uniform cooling reduces  $U_{top}$  and eliminates bifurcations that would occur with uniform cooling. Heating has the opposite effect, as it lowers the critical Rayleigh number and increases the achievable  $U_{top}$ .

The type of fluid strongly affects the magnitude of  $U_{top}$ . The propulsive effect relies on horizontal temperature gradients, which diminish with an increase of  $Pr$  as this leads to more intense convection resulting in a reduction of these gradients. The thermal streaming and drift are affected similarly, as illustrated in figures 5(b) and 7(b). The cumulative effect is shown in figure 13. Reduction of  $Pr$  reduces the critical Rayleigh number and increases the magnitude of  $U_{top}$ . A slight increase of Prandtl number from  $Pr = 0.71$  to  $Pr = 1$  eliminates bifurcations and leads to a significant reduction of  $U_{top}$ .

Stability analysis was carried out using the formulation described in Appendix A. No unstable eigenvalues have been found, which suggests that the flows generated by the combined thermal streaming and thermal drift reported here are stable.

## 6. Summary

Analysis of the propulsive effect generated by heated grooves has been carried out. The model problem consists of parallel horizontal plates with the upper plate free to move

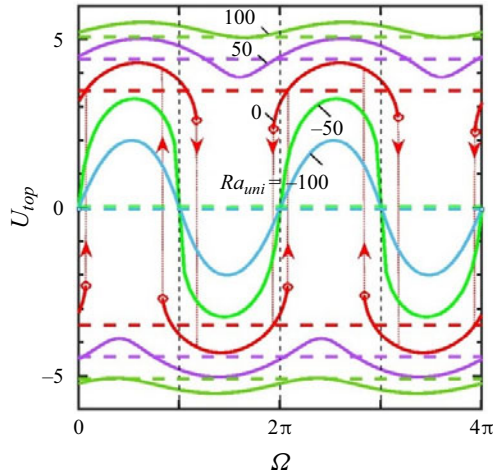


Figure 12. Variations of the upper plate velocity  $U_{top}$  as a function of the phase shift  $\Omega$  for  $\alpha = 2$ ,  $A = 0.025$ ,  $Ra_{per} = 1000$ ,  $Pr = 0.71$  and  $Ra_{uni} = -100, -50, 0, 50, 100$ . Circles identify limit points. Dashed lines provide the plate velocity achieved with smooth plates. Positions of limit points were determined using stability theory.

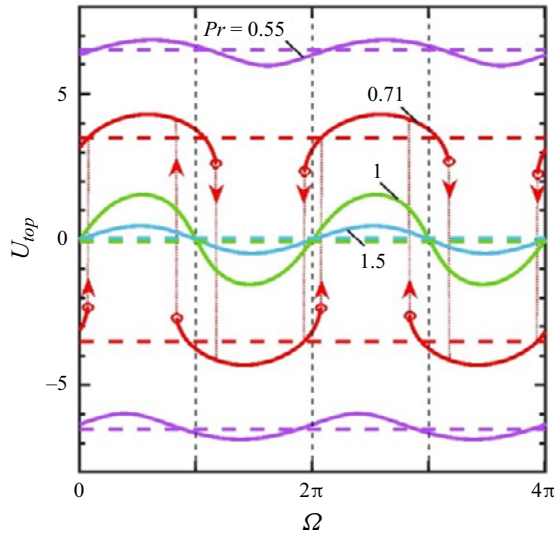


Figure 13. Variations of the upper plate velocity  $U_{top}$  as a function of the phase shift  $\Omega$  for  $\alpha = 2$ ,  $A = 0.025$ ,  $Ra_{uni} = 0$ . Here,  $Ra_{per} = 1000$  for  $Pr = 0.55, 0.71, 1, 1.5$ . Circles identify limit points. Dashed lines provide the plate velocity achieved with smooth plates. Positions of limit points were determined using stability theory.

and the lower plate equipped with grooves and subject to periodic heating. Perfectly tuned sinusoidal groove and heating patterns were considered, i.e. the same wavenumber described them. Heating forced movement of the upper plate whose velocity was used to measure propulsion effectiveness.

Two effects contribute to propulsion. The first effect is produced by an interaction of groove and heating patterns creating a thermal drift representing a forced system response. The strength of this effect depends on the relative position of both patterns. The upper plate movement reaches the maximum when hot spots are located approximately half-way



between the groove peaks and troughs. It changes direction depending if the hot spot is on the right or left side of the groove peak. Thermal drift disappears when the hot spots are located at the groove peaks or the groove troughs.

The second effect relies on nonlinear thermal streaming and requires sufficiently intense heating for its activation. This effect represents system bifurcation. Both the thermal drift and the nonlinear streaming are active simultaneously and generate plate movement regardless of the relative position of both patterns. Similar to pure thermal drift, the fastest plate movement occurs for hot spots half-way between the groove peaks and troughs. A somewhat slower movement results when hot spots are located near the groove peaks and troughs. Under such conditions, the direction and velocity of plate movement may change drastically in response to a slight change in the relative position of both patterns. The formation of limit points and hysteresis loops was observed in response to changes in the relative position of both patterns.

The magnitude of propulsion increases with a decrease in the Prandtl number and expands with the addition of a uniform heating component. Despite extensive testing, investigating the stability of flows generated by the heating failed to identify any unstable eigenvalue.

**Funding.** This work was carried out with the support of NSERC of Canada.

**Declaration of interests.** The authors report no conflict of interest.

**Author ORCIDs.**

 J.M. Floryan <http://orcid.org/0000-0003-3296-4122>;

 S. Panday <http://orcid.org/0000-0001-7120-683X>.

## Appendix A. Linear stability analysis

The analysis begins with the governing equations expressed in terms of the vorticity transport, energy and continuity equations in the following form:

$$\frac{\partial \boldsymbol{\omega}}{\partial t} - (\boldsymbol{\omega} \cdot \nabla) \mathbf{V} + (\mathbf{V} \cdot \nabla) \boldsymbol{\omega} = \nabla^2 \boldsymbol{\omega} + \nabla \times (Pr^{-1} \theta \mathbf{j}), \quad (\text{A1a})$$

$$\frac{\partial \theta}{\partial t} + (\mathbf{V} \cdot \nabla) \theta = Pr^{-1} \nabla^2 \theta, \quad (\text{A1b})$$

$$\nabla \cdot \mathbf{V} = 0, \quad \boldsymbol{\omega} = \nabla \times \mathbf{V}, \quad (\text{A1c,d})$$

where  $\mathbf{V} = (u, v, w)$  is the velocity vector,  $\boldsymbol{\omega} = (\xi, \eta, \phi)$  is the vorticity vector and  $\theta$  stands for the temperature. We superimpose unsteady, three-dimensional infinitesimal disturbances onto the primary flow discussed in the main body of the paper and represent the flow, vorticity and temperature fields as

$$\mathbf{V} = \mathbf{v}_B(x, y) + \mathbf{v}_D(x, y, z, t), \quad \theta = \theta_B(x, y) + \theta_D(x, y, z, t). \quad (\text{A2a,b})$$

The subscripts  $B$  and  $D$  above refer to the heating-modified flow (basic state) described in the main body of this paper and disturbances, respectively. Substitution of (A2) into (A1), subtraction of the basic state quantities and linearization of the resulting equations leads



to the disturbance equations of the form

$$\begin{aligned} \frac{\partial \boldsymbol{\omega}_D}{\partial t} - (\boldsymbol{\omega}_B \cdot \nabla) V_D - (\boldsymbol{\omega}_D \cdot \nabla) V_B + (V_B \cdot \nabla) \boldsymbol{\omega}_D + (V_D \cdot \nabla) \boldsymbol{\omega}_B \\ = \nabla^2 \boldsymbol{\omega}_D + \nabla \times (Pr^{-1} \theta_D \mathbf{g}_j), \end{aligned} \quad (\text{A3a})$$

$$\frac{\partial \theta_D}{\partial t} + (V_B \cdot \nabla) \theta_D + (V_D \cdot \nabla) \theta_B = Pr^{-1} \nabla^2 \theta_D, \quad \nabla \cdot V_D = 0, \quad \boldsymbol{\omega}_D = \nabla \times V_D, \quad (\text{A3b-d})$$

where  $\mathbf{j}$  is the unit vector along the vertical  $y$ -direction. The relevant boundary conditions have the form

$$y = 1: u_{D,per} = \left. \frac{\partial u_D}{\partial y} \right|_{mean} = v_D = w_D = \theta_D = 0, \quad (\text{A4a})$$

$$y = y_L: u_D = v_D = w_D = \theta_D = 0. \quad (\text{A4b})$$

System (A3)–(A4) defines a linear stability problem for the spatially modulated flow with modulations characterized by the wavenumber  $\alpha$ . The disturbances are represented as

$$[V_D, \boldsymbol{\omega}_D, \theta_D](x, y, z, t) = [\mathbf{G}_D, \boldsymbol{\Omega}_D, \kappa_D](x, y) e^{i(\delta x + \mu z - \sigma t)} + \text{c.c.}, \quad (\text{A5})$$

where  $\sigma = \sigma_r + i\sigma_i$  is the complex frequency with  $\sigma_i$  describing the rate of growth of disturbances and  $\sigma_r$  describing their frequency and c.c. stands for the complex conjugate. Here,  $\mathbf{G}_D(x, y)$ ,  $\boldsymbol{\Omega}_D(x, y)$  and  $\kappa_D(x, y)$  are the  $x$ -periodic amplitude functions accounting for the spatial flow modulations.

The spatial distribution of disturbances is characterized by the spanwise ( $\mu$ ) and streamwise ( $\delta$ ) wavenumbers, with their amplitude functions being periodic in  $x$ . The former completely characterizes the overall system periodicity in the spanwise direction, while its periodicity in the longitudinal direction depends on the ratio of  $\alpha$  and  $\delta$ . The system can be aperiodic in this direction for an irrational ratio of  $\alpha$  and  $\delta$  (incommensurable system) and could be periodic but with wavelengths varying by several orders of magnitude (commensurable systems). Wavenumber  $\alpha$  is a control parameter as its value characterizes heating and topography patterns and can be selected arbitrarily. The stability analysis requires consideration of all possible  $\delta$  values for a given  $\alpha$ , which gives rise to commensurability effects. It also requires consideration of all possible  $\mu$  values, but this does not lead to commensurability effects. Here, we follow the formulation proposed by Floryan (1997, 2002), which properly handles commensurability; see also Panday & Floryan (2023).

Substitutions of (A5) into (A3) lead to the partial differential equations for the amplitude functions. Since these functions are  $x$ -periodic, they can be expressed in terms of Fourier expansions of the form

$$\mathbf{G}_D(x, y) = \sum_{m=-N_D}^{+N_D} [g_u^{(m)}(y), g_v^{(m)}(y), g_w^{(m)}(y)] e^{im\alpha x} + \text{c.c.}, \quad (\text{A6a})$$

$$\boldsymbol{\Omega}_D(x, y) = \sum_{m=-N_D}^{+N_D} [g_\xi^{(m)}(y), g_\eta^{(m)}(y), g_\phi^{(m)}(y)] e^{im\alpha x} + \text{c.c.}, \quad (\text{A6b})$$

$$\kappa_D(x, y) = \sum_{m=-N_D}^{+N_D} [g_\theta^{(m)}(y)] e^{im\alpha x} + \text{c.c.}, \quad (\text{A6c})$$

where  $g_u^{(m)}(y)$ ,  $g_v^{(m)}(y)$ ,  $g_w^{(m)}(y)$ ,  $g_\xi^{(m)}(y)$ ,  $g_\eta^{(m)}(y)$ ,  $g_\phi^{(m)}(y)$ ,  $g_\theta^{(m)}(y)$  stand for the modal functions and  $N_D$  is the number of Fourier modes retained in the Fourier expansions used to represent disturbance quantities. The basic state flow quantities are also expressed as Fourier expansions, i.e.

$$[u_B, v_B, \theta_B](x, y) = \sum_{n=-N_B}^{N_B} [f_u^{(m)}, f_v^{(m)}, f_\theta^{(m)}](y) e^{im\alpha x}, \tag{A7}$$

where  $N_B$  denotes the number of Fourier modes retained in the representation of the basic state. Substitution of (A6)–(A7) into the partial differential equations for the amplitude functions, elimination of  $g_u^{(m)}(y)$  and  $g_w^{(m)}(y)$  and separation of Fourier modes leads to the ordinary differential equations for the modal functions for  $g_v^{(m)}(y)$ ,  $g_\eta^{(m)}(y)$  and  $g_\theta^{(m)}(y)$  of the form

$$T^{(m)} g_v^{(m)} - Pr^{-1} k_m^2 g_\theta^{(m)} = \sum_{n=-N_M}^{N_M} [(T_1^{(m-n)} + T_2^{(m-n)} + T_3^{(m-n)}) g_v^{(m-n)} + (T_4^{(m-n)} - T_5^{(m-n)}) g_\eta^{(m-n)}], \tag{A8a}$$

$$S^{(m)} g_\eta^{(m)} = \sum_{n=-N_M}^{+N_M} [(S_1^{(m-n)} + S_2^{(m-n)} + S_3^{(m-n)}) g_v^{(m-n)} + (S_4^{(m-n)} - S_5^{(m-n)}) g_\eta^{(m-n)}], \tag{A8b}$$

$$Q^{(m)} g_\theta^{(m)} = \sum_{n=-N_M}^{+N_M} \left[ Q_1^{(m-n)} g_\theta^{(m-n)} + Q_2^{(m-n)} g_v^{(m-n)} + \frac{\mu n \alpha f_\theta^{(n)}}{k_{m-n}^2} g_\eta^{(m-n)} \right], \tag{A8c}$$

where

$$D^q = \frac{d^q}{dy^q}, \tag{A9}$$

$$t_m = \delta + m\alpha, \tag{A10}$$

$$k_m^2 = t_m^2 + \mu^2, \tag{A11}$$

$$T^{(m)} = (D^2 - k_m^2)^2 + i\sigma(D^2 - k_m^2), \tag{A12}$$

$$S^{(m)} = (D^2 - k_m^2) + i\sigma, \tag{A13}$$

$$Q^{(m)} = Pr^{-1}(D^2 - k_m^2) + i\sigma, \tag{A14}$$

$$T_1^{(m-n)} = \frac{it_{m-n}}{k_{m-n}^2} (-t_m^2 D f_u^{(n)} D + in\alpha k_m^2 f_v^{(n)} D - t_m^2 f_u^{(n)} D^2 + it_m D f_v^{(n)} D^2 + it_m f_v^{(n)} D^3), \tag{A15}$$

$$T_2^{(m-n)} = ik_m^2 t_{m-n} f_u^{(n)} + k_m^2 D f_v^{(n)} + k_m^2 f_v^{(n)} D + it_m D^2 f_u^{(n)} + it_m D f_u^{(n)} D, \tag{A16}$$

$$T_3^{(m-n)} = \frac{i\mu}{k_{m-n}^2} (-\mu t_{m-2n} f_u^{(n)} D^2 + i\mu f_v^{(n)} D^3 - \mu t_{m-n} D f_u^{(n)} D), \tag{A17}$$

$$T_4^{(m-n)} = \frac{it_{m-n}}{k_{m-n}^2} (-\mu t_{m-2n} f_u^{(n)} D + i\mu f_v^{(n)} D^2 - \mu t_{m-n} D f_u^{(n)}), \tag{A18}$$

*Use of heated corrugations for propulsion*

$$T_5^{(m-n)} = \frac{i\mu}{k_{m-n}^2} (-t_m^2 D f_u^{(n)} + i n \alpha k_m^2 f_v^{(n)} - t_m^2 f_u^{(n)} D + i t_m D f_v^{(n)} D + i t_m f_v^{(n)} D^2), \quad (\text{A19})$$

$$S_1^{(m-n)} = \frac{i\mu}{k_{m-n}^2} (t_{m-n} t_m f_u^{(n)} D - i t_m f_v^{(n)} D^2), \quad (\text{A20})$$

$$S_2^{(m-n)} = i\mu D f_u^{(n)}, \quad (\text{A21})$$

$$S_3^{(m-n)} = \frac{i t_{m-n}}{k_{m-n}^2} (i\mu f_v^{(n)} D^2 - \mu t_m f_u^{(n)} D), \quad (\text{A22})$$

$$S_4^{(m-n)} = \frac{i t_{m-n}}{k_{m-n}^2} (t_{m-n} t_m f_u^{(n)} - i t_m f_v^{(n)} D), \quad (\text{A23})$$

$$S_5^{(m-n)} = \frac{i\mu}{k_{m-n}^2} (i\mu f_v^{(n)} D - \mu t_m f_u^{(n)}), \quad (\text{A24})$$

$$Q_1^{(m-n)} = i t_{m-n} f_u^{(n)} + f_v^{(n)} D, \quad (\text{A25})$$

$$Q_2^{(m-n)} = D f_\theta^{(n)} - \frac{n \alpha f_\theta^{(n)} t_{m-n}}{k_{m-n}^2} D. \quad (\text{A26})$$

Modal functions are coupled due to spatial flow modulations and due to the geometry of the bounding walls. These functions were expressed using Chebyshev expansions, and the Galerkin projection method was used to construct a matrix eigenvalue problem involving expansion coefficients. The boundary conditions for the modal functions were expressed as constraints using the immersed boundary conditions concept (Szumbarski & Floryan 1999; Panday & Floryan 2023). These constraints were implemented using the tau method (Canuto *et al.* 1992), i.e. entries in the matrix corresponding to the highest Chebyshev polynomials were replaced by constraints. The resulting eigenvalue problem was solved using standard techniques. The overall solution method provides spectral accuracy for eigenvalues and eigenfunctions.

REFERENCES

- ABTAHI, A. & FLORYAN, J.M. 2017 Natural convection and thermal drift. *J. Fluid Mech.* **826**, 553–582.
- ABTAHI, A. & FLORYAN, J.M. 2018 On the formation of thermal drift. *Phys. Fluids* **30**, 043602.
- ALI, N., ULLAH, K. & RASOOL, H. 2020 Bifurcation analysis for a two-dimensional peristaltic driven flow of power-law fluid in asymmetric channel. *Phys. Fluids* **32**, 073104.
- BEWLEY, T.R. 2009 A fundamental limit on the balance of power in a transpiration-controlled channel flow. *J. Fluid Mech.* **632**, 443–446.
- BLAKE, J.R. & SLEIGH, M.A. 1974 Mechanics of ciliary locomotion. *Biol. Rev.* **49**, 85–125.
- BRENNEN, C. & WINET, H. 1977 Fluid mechanics of propulsion by cilia and flagella. *Annu. Rev. Fluid Mech.* **9**, 339–398.
- CANUTO, C., HUSSAINI, M.Y., QUARTERONI, A. & ZANG, T.A. 1992 *Spectral Methods in Fluid Dynamics*. Springer.
- CATTAFESTA, L.N. & SHEPLAK, M. 2011 Actuators for active flow control. *Annu. Rev. Fluid Mech.* **43**, 247–272.
- CHAN, B., BALMFORTH, N.J. & HOSOI, A.E. 2005 Lubrication and adhesive locomotion. *Phys. Fluids* **19**, 113101.
- FLORYAN, D. 2023 A fundamental limit on energy savings in controlled channel flow, and how to beat it. *J. Fluid Mech.* **954**, R3.
- FLORYAN, D., BUREN, T.V. & SMITS, A.J. 2018 Efficient cruising for swimming and flying animals is dictated by fluid drag. *PNAS* **115**, 8116–8118.
- FLORYAN, D. & FLORYAN, J.M. 2015 Drag reduction in heated channels. *J. Fluid Mech.* **765**, 353–395.

- FLORYAN, J.M. 1997 Stability of wall bounded shear layers with simulated distributed surface roughness. *J. Fluid Mech.* **335**, 29–55.
- FLORYAN, J.M. 2002 Centrifugal instability of Couette flow over a wavy-wall. *Phys. Fluids* **14**, 312–322.
- FLORYAN, J.M., FAISAL, M. & PANDAY, S. 2021 On the peristaltic pumping. *Phys. Fluids* **33**, 033609.
- FLORYAN, J.M. & HAQ, N. 2022 Use of vibrations for reduction of resistance in relative movement of parallel plates. *J. Fluid Mech.* **949**, A28.
- FLORYAN, J.M., HAQ, N. & PANDAY, S. 2022a Horizontal chimney effect. *ASME J. Heat Transfer* **144** (072601), 1–8.
- FLORYAN, J.M. & INASAWA, A. 2021 Pattern interaction effect. *Sci. Rep.* **11**, 14573.
- FLORYAN, J.M., PANDAY, S. & AMAN, S.A. 2022b Propulsion due to thermal streaming. *J. Fluid Mech.* **967**, A13.
- FLORYAN, J.M., SHADMAN, S. & HOSSAIN, M.Z. 2018 Heating-induced drag reduction in relative movement of parallel plates. *Phys. Rev. Fluids* **3**, 094102.
- FUKAGATA, K., SUGIYAMA, K. & KASAGI, N. 2009 On the lower bound of net driving power in controlled duct flows. *Physica D* **338**, 1082–1086.
- FUKUNISHI, Y. & EBINA, I. 2001 Active control of boundary-layer transition using a thin actuator. *JSME Intl J.* **44**, 24–29.
- FUNG, Y.C. & YIH, C.S. 1968 Peristaltic transport. *J. Appl. Mech.* **35**, 669–675.
- GEPNER, S.W. & FLORYAN, J.M. 2020 Use of surface corrugations for energy-efficient chaotic stirring in Low Reynolds number flows. *Sci. Rep.* **10**, 1–8.
- HAQ, N. & FLORYAN, J.M. 2022 Propulsive effect of wall vibrations. *ASME J. Fluid Engng* **144**, 121204-1–121204-11.
- HOEPPFNER, J. & FUKAGATA, K. 2009 Pumping or drag reduction. *J. Fluid Mech.* **635**, 171–187.
- HOSSAIN, M.Z. & FLORYAN, J.M. 2013 Instabilities of natural convection in a periodically heated layer. *J. Fluid Mech.* **733**, 33–67.
- HOSSAIN, M.Z. & FLORYAN, J.M. 2016 Drag reduction in a thermally modulated channel. *J. Fluid Mech.* **791**, 122–153.
- HOSSAIN, M.Z. & FLORYAN, J.M. 2020 On the role of surface grooves in the reduction of pressure losses in heated channels. *Phys. Fluids* **32**, 083610.
- HOSSAIN, M.Z. & FLORYAN, J.M. 2022 Wavenumber lock-in and spatial parametric resonance in convection. *J. Fluid Mech.* **944**, A47.
- HOSSAIN, M.Z., FLORYAN, D. & FLORYAN, J.M. 2012 Drag reduction due to spatial thermal modulations. *J. Fluid Mech.* **713**, 398–419.
- HUSAIN, S.Z. & FLORYAN, J.M. 2008 Implicit spectrally-accurate method for moving boundary problems using immersed boundary conditions concept. *J. Comput. Phys.* **227**, 4459–4477.
- HUSAIN, S.Z. & FLORYAN, J.M. 2010 Spectrally-accurate algorithm for moving boundary problems for the Navier–Stokes equations. *J. Comput. Phys.* **229**, 2287–2313.
- HUSAIN, S.Z., SZUMBARSKI, J. & FLORYAN, J.M. 2009 Over-determined formulation of the immersed boundary condition method. *Comput. Meth. Appl. Mech. Engng* **199**, 94–112.
- INASAWA, A., HARA, K. & FLORYAN, J.M. 2021 Experiments on thermal drift. *Phys. Fluids* **33**, 087116.
- INASAWA, A., TANEDA, K. & FLORYAN, J.M. 2019 Experiments on flows in channels with spatially distributed heating. *J. Fluid Mech.* **872**, 177–197.
- INASAWA, I., NINOMIYA, C. & ASAI, M. 2013 Suppression of tonal trailing-edge noise from an airfoil using a plasma actuator. *AIAA J.* **51**, 1695–1702.
- JAFFRIN, M.Y. & SHAPIRO, A.H. 1971 Peristaltic pumping. *Annu. Rev. Fluid Mech.* **3**, 13–37.
- JIAO, L. & FLORYAN, J.M. 2021a On the use of transpiration for reduction of resistance to relative movement of parallel plates. *Phys. Rev. Fluids* **6**, 014101.
- JIAO, L. & FLORYAN, J.M. 2021b On the use of transpiration patterns for reduction of pressure losses. *J. Fluid Mech.* **915**, A78.
- KATO, T., FUKUNISHI, F. & KOBAYASHI, R. 1997 Artificial control of the three-dimensionalization process of T–S waves in boundary-layer transition. *JSME Intl J.* **640**, 536–541.
- KATZ, D.F. 1974 On the propulsion of micro-organisms near solid boundaries. *J. Fluid Mech.* **64**, 33–49.
- LAUGA, E. 2016 Bacterial hydrodynamics. *Annu. Rev. Fluid Mech.* **48**, 105–135.
- LEE, S., BUSH, J.W.W., HOSOI, A.E. & LAUGA, E. 2008 Crawling beneath the free surface: water snail locomotion. *Phys. Fluids* **20**, 082106.
- MANNAM, N.P.B. & KRISHNANKUTTY, P. 2019 *Propulsion Systems: Biological Propulsion Systems for Ships and Underwater Vehicles*. IntechOpen.
- MOHAMMADI, A. & FLORYAN, J.M. 2013a Pressure losses in grooved channels. *J. Fluid Mech.* **725**, 23–54.
- MOHAMMADI, A. & FLORYAN, J.M. 2013b Groove optimization for drag reduction. *Phys. Fluids* **25**, 113601.

## *Use of heated corrugations for propulsion*

- MOHAMMADI, A. & FLORYAN, J.M. 2015 Numerical analysis of laminar-drag-reducing grooves. *ASME J. Fluids Engng* **137**, 041201.
- MORADI, H.V. & FLORYAN, J.M. 2013 Flows in annuli with longitudinal grooves. *J. Fluid Mech.* **716**, 280–315.
- PANDAY, S. & FLORYAN, J.M. 2021 An algorithm for analysis of pressure losses in heated channels. *Intl J. Numer. Meth. Fluids* **93**, 1332–1358.
- PANDAY, S. & FLORYAN, J.M. 2023 Accurate determination of stability characteristics of spatially modulated shear layers. *J. Fluid Mech.* **975**, A50.
- SHAPIRO, S., JAFFRIN, M. & WEINBERG, S. 1969 Peristaltic pumping with long wavelengths at low Reynolds numbers. *J. Fluid Mech.* **37**, 799–825.
- SMITS, A.J. 2019 Undulatory and oscillatory swimming. *J. Fluid Mech.* **874**, P1.
- SZUMBARSKI, J. & FLORYAN, J.M. 1999 A direct spectral method for determination of flows over corrugated boundaries. *J. Comput. Phys.* **153**, 378–402.
- TAYLOR, G. 1951 Analysis of the swimming of microscopic organisms. *Proc. R. Soc. Lond. A* **209**, 447–461.
- TRITTON, D.J. 1977 *Physical Fluid Dynamics*. Van Nostrand.
- WALSH, M.J. 1983 Riblets as a viscous drag reduction technique. *AIAA J.* **21**, 485–486.
- WU, T.Y. 2011 Fish swimming and bird/insect flight. *Annu. Rev. Fluid Mech.* **43**, 25–58.